RSC Advances

PAPER

View Article Online
View Journal | View Issue

Cite this: *RSC Adv.*, 2026, **16**, 11752

Peroxymonosulfate activation by a nitrogen-doped multilayer graphene catalyst derived from cotton for enhanced flurbiprofen degradation

Rui Sun,[a] Yanfei Chen,[b] Limeng Yang,[c] Zhi Zhu,[a] Zhaohua Zheng[a] and Li Sun *[a]

Received 16th December 2025
Accepted 19th February 2026

DOI: 10.1039/d5ra09729k

rsc.li/rsc-advances

Recalcitrant pharmaceuticals and personal care products (PPCPs) like flurbiprofen often elude conventional wastewater treatments, posing significant environmental risks that necessitate innovative solutions. Advanced oxidation processes based on sulfate radicals ($^{\bullet}SO_4^-$) from activated peroxymonosulfate (PMS) can facilitate the thorough degradation of PPCPs in wastewater thanks to their superior oxidation potential. This study developed a nitrogen-doped multilayer graphene catalyst, INC_{II}, from cotton fibers *via* template-assisted pyrolysis. Sodium chloride was used as the hard template, facilitating easy template removal and avoiding usage of hazardous hydrofluoric acid. A nitrogen-containing ionic liquid [EMIm][$N(CN)_2$] was employed as the nitrogen source. With 0.5 g L^{-1} of the INC_{II} catalyst and 6 mM of PMS, the flurbiprofen removal rate reached approximately 94.9% (initial concentration = 20 mg L^{-1}), surpassing all previously reported work. Pyridinic nitrogen proved the most potent active site for PMS activation. By incorporating waste cotton fibers into the pharmaceutical wastewater treatment solution, this study offers a practical approach to biomass recycling and an actionable reference for treating waste with waste.

Introduction

A large volume of wastewater containing pharmaceuticals and personal care products (PPCPs) is generated during production and consumption. Yet, most urban sewage treatment plants lack dedicated PPCP treatment processes at present. Ineffective PPCP removal *via* conventional water treatment results in PPCP pollutants remaining in the treated water, such as flurbiprofen (Fig. 1), an anti-inflammatory and analgesic drug.[1] Due to its physiological activities, flurbiprofen may adversely affect various aquatic ecosystems.[2] For one thing, traditional water treatment prioritizes sensory quality and microbial safety rather than PPCP removal. For another, the diverse chemical structures of PPCPs often render single-process solutions ineffective. Specifically, the coagulation-sedimentation process cannot adsorb small-molecule, highly water-soluble PPCPs. Filtration cannot retain PPCPs in the residual, and conventional activated carbon filters saturate quickly. Chlorine and UV disinfection can sterilize but cannot fully degrade PPCPs or prevent the formation of more toxic byproducts.[3] Limited by their pollutant-focused design, conventional water treatment processes can rarely achieve improved PPCP removal through parameter adjustments. Thus, advanced oxidation processes (AOPs) have become essential for the co-removal of conventional pollutants and PPCPs. Among them, sulfate radical-based AOPs show promise for complete PPCP degradation.

With a greater selectivity and a broader pH range, sulfate radical ($^{\bullet}SO_4^-$)-based AOPs enable the rapid decomposition of PPCP molecules into carbon dioxide and water.[4] This process typically utilizes a catalyst to activate peroxymonosulfate (HSO_5^-, PMS), which generates the strong oxidizing $^{\bullet}SO_4^-$ radicals to degrade pollutants.[5] Numerous high-performance catalysts have been developed in recent years, including graphitic carbon nitride nanocomposites,[6,7] carbon dots,[8] and porous nanocrystalline materials.[9,10] Non-metallic nitrogen-doped carbon catalysts are primarily prepared by incorporating nitrogen atoms or nitrogen-containing functional groups into carbon materials *via* pyrolysis.[11] Recently, nitrogen-doped carbon catalysts have been widely applied in PMS activation due to their remarkable catalytic performance. Qiu *et al.*[12] used

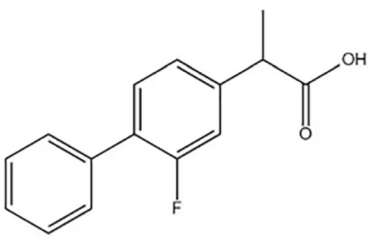

Fig. 1 Chemical structure of flurbiprofen.

[a]*Department of Digestive Surgery, Honghui Hospital, Xi'an Jiaotong University, Xi'an 710054, China. E-mail: hhsl_11@163.com*

[b]*Department of Spine Surgery, Honghui Hospital, Xi'an Jiaotong University, Xi'an 710054, China*

[c]*School of Textile Science & Engineering, Xi'an Polytechnic University, Xi'an 710048, China*

SBA-15 mesoporous molecular sieve as a template and BMIM-dca as a precursor to prepare nitrogen-containing mesoporous carbon. As a simple carbonization pretreatment, the template method demonstrated the great application potential of ionic liquids (ILs) in synthesizing nitrogen-doped carbon materials. However, hard template removal often requires washing with pickling acids (*e.g.*, hazardous hydrofluoric acid). To overcome this drawback, NaCl and/or $ZnCl_2$ salts, which can be removed by water washing, were used as templates to fabricate high-surface-area, nitrogen-doped functional carbons.[13]

Meanwhile, PMS activation poses various challenges. Nanocatalysts tend to agglomerate, which reduces the exposure of active sites and diminishes catalytic efficiency.[14] The recovery and reuse of most catalysts are difficult, often requiring additional centrifugation or filtration before subsequent applications.[15] Cotton fibers represent highly cost-effective precursors with large aspect ratios, outstanding physical properties, and high processability.[16] In addition, their high cellulose and carbon content make them ideal candidates for the preparation of bio-based carbon materials.[17] Using cotton fibers as precursors, nitrogen-doped carbon catalysts demonstrated improved PMS activation performance for the removal of reactive dyes and emerging pollutants.[18] However, few considered the characteristics of cotton itself. Scholars have studied the pollutant degradation performance of PMS activated by various catalysts with different crystalline cotton fibers as biocarbon precursors, linking the final catalyst properties to the different crystal forms of cellulose.[17]

This study prepares a novel nitrogen-doped carbon catalyst for activating PMS to degrade flurbiprofen, using modified cotton as a precursor and a nitrogen-containing IL as the nitrogen source. The performance of flurbiprofen degradation *via* PMS activation is evaluated. 1-Ethyl-3-methylimidazolium dicyanamide ([EMIm][$N(CN)_2$]) is selected due to its high carbon and nitrogen content.[19] Flurbiprofen, a common anti-inflammatory drug frequently detected in wastewater, is selected as the target pollutant considering its stable structure and the limited research on its degradation.[20] The adaptability, stability, and versatility of the nitrogen-doped carbon catalyst are evaluated. The ecotoxicity of degradation intermediates and treated effluents is assessed using the Toxic Estimation Software Tool (TEST) and mung bean phytotoxicity assays to check whether the INC_{II} catalyst/PMS system is low-toxic and eco-friendly. This application of waste cotton fibers for PPCP wastewater treatment represents a practical approach for biomass recycling.

Experimental

Materials and chemicals

The waste cotton fibers were acquired from Xi'an Textile Group Co, Ltd (Xi'an, China). The analytical chemicals included [EMIm][$N(CN)_2$] ($C_8H_{11}N_5$, denoted as IL), NaCl, sodium hydroxide (NaOH), ethylenediamine ($C_2H_8N_2$), glycerin ($C_3H_8O_3$), methanol (CH_3OH), acetone (C_3H_6O), flurbiprofen ($C_{15}H_{13}FO_2$), and potassium peroxymonosulfonate ($H_3K_5O_{18}S_4$). Deionized water (18.2 MΩ cm) produced by a Millipore water system (Synergy®UV, France) was used in all experiments.

Carbonization of modified cotton fibers

First, the waste cotton fibers were thoroughly washed with a detergent and deionized water at least three times to remove visible contaminants. Subsequently, cotton cellulose I_β (C-I)[22] was isolated after removing impurities like textile sizes by immersing the cleaned cotton fibers in a 0.5 M NaOH solution (1 : 50 bath ratio) at 100 °C for 30 min. Next, the fibers were repeatedly washed with deionized water until neutral and then dried at 80 °C.

Cotton cellulose II (C-II) fibers were prepared by soaking the C-I fibers in a 18.5% NaOH solution for 1.5 h, washing with a large volume of deionized water until neutral, and then freeze-drying.

The modified cotton fibers C-II (5 g) were placed in a quartz tubular furnace for pyrolysis. After evacuating to −0.02 MPa, inert Ar gas was introduced. Then, the sample was heated to 800 °C at 5 °C min^{-1} and pyrolyzed for 2 h. After cooling to room temperature, carbonized modified cotton fibers were obtained for later use as the carbon precursor.

Preparation of nitrogen-doped multilayer graphene catalysts

Briefly, the carbonized C-II was soaked in a saturated NaCl solution, and the mixture was heated to 80 °C in an oil bath to evaporate all the water. The IL ([EMIm][$N(CN)_2$]), NaCl, and carbonized C-II in a weight proportion of 10 : 5 : 1 were thoroughly ground and placed for pyrolysis. The precursors were heated to 900 °C at 5 °C min^{-1} and pyrolyzed for 2 h unless otherwise stated. The mixture was washed three times with deionized water to remove the NaCl template after cooling. Different types of nitrogen-doped carbon catalysts were obtained using cotton fibers C-I, modified cotton fibers C-II, or uncarbonized modified cotton fibers $C_{II\text{-}UC}$ and recorded as INC_x (x = I, II, II-UC). In addition, the catalyst obtained by pyrolysis of cotton fibers C-II at 900 °C was recorded as CC_{II}, and the catalyst obtained by pyrolysis of the pure IL at 900 °C was recorded as CILs. The catalyst prepared without IL was denoted NC_{II}, the catalyst without any cotton fibers was denoted IN, and the one without the NaCl template was denoted IC_{II}. After four runs of degradation, the used catalyst was collected and retreated at 900 °C to obtain the regenerated catalyst, denoted as the regenerated INC_{II} catalyst. The synthetic routes for the nitrogen-doped carbon catalysts are shown in Fig. 2.

Catalytic performance evaluation

The flurbiprofen degradation performance was tested in a 250 mL beaker at room temperature (25 °C). The effects of pH and temperature on flurbiprofen degradation were also investigated. The pH of the reaction mixture was adjusted using 0.1 M H_2SO_4 and 0.1 M NaOH. Unless otherwise specified, the pH and temperature of the reaction system were not further regulated. First, the catalyst to be evaluated was added to a 120 mL flurbiprofen solution, and an adsorption equilibrium was achieved within approximately 0.5 h. Subsequently,

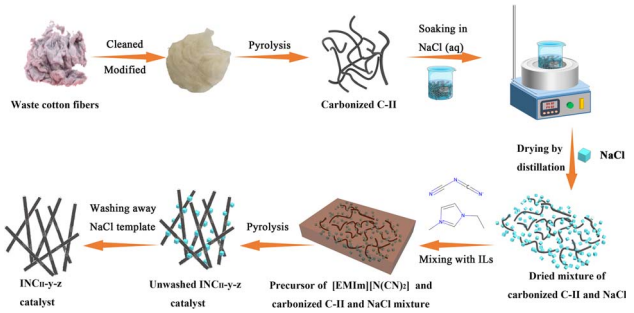

Fig. 2 Synthetic route of the nitrogen-doped carbon catalyst derived from modified cotton and metal-free IL.

a certain amount of PMS was added to the flurbiprofen solution, and the mixture was stirred continuously for 90 min. At 0, 10, 20, 30, 50, 70, and 90 min, 4 mL of flurbiprofen solution was extracted from the reaction mixture using a 0.22 μm syringe filter, and 0.5 mL of methyl alcohol was added. Flurbiprofen concentration was measured using high-performance liquid chromatography-mass spectrometry (HPLC-MS Agilent 6530 TOF) with a UV-vis detector at 248 nm. The HPLC-MS test conditions and analytical methods are detailed in Text S1. A first-order kinetic model was applied to evaluate the degradation kinetics of flurbiprofen, as expressed by eqn (1):

$$\ln C_t/C_0 = -k \cdot t \quad (1)$$

where C_t and C_0 are the flurbiprofen concentration at t (min) and $t = 0$, respectively, and k denotes the reaction rate constant. The activation energy can be calculated using the Arrhenius Equation:

$$\ln k = \ln A - E_a/RT \quad (2)$$

where A indicates a constant, E_a denotes the activation energy (J mol^{-1}), R represents the universal gas constant (8.314 J mol^{-1} K^{-1}), and T denotes the reaction temperature.

In addition, four quenching agents, namely, methanol (MeOH), *tert*-butanol (TBA), chloroform (CF), L-histidine (L-His), and dimethylsulfoxide (DMSO), were employed to determine the active substances that degrade flurbiprofen. 5,5-Dimethyl-1-pyrroliane *n*-oxide (DMPO) and 2,2,6,6-tetramethyl-4-piperidone (TEMP) were used as spin trapping agents. In the mixture with PMS (6 mM) and INC_{II} (0.5 g L^{-1}), free radicals were detected by electron paramagnetic resonance (EPR) spectroscopy, and the reactive oxygen species (ROS) in the system were identified.

Characterization methods

The material morphology was observed using an Oxford Quanta 400 F field-emission scanning electron microscope (FESEM) at an acceleration voltage of 20 kV. Energy dispersive spectroscopy (EDS) was also conducted on the FESEM. X-ray diffraction (XRD) was carried out on a Rigaku MiniFlex 300/600 with a 2θ in the range of 5° to 90° and a scanning speed of 5°·min^{-1}. The mass loss of cotton cellulose/urea precursors during pyrolysis was evaluated through thermogravimetric analysis (TGA) and derivative thermogravimetry (DTG) with a NETZSCH STA 449 C thermal analyzer in a temperature range of 30 °C to 1000 °C. The Ar gas flow rate was set at 10 mL min^{-1}, and the heating rate was maintained at 5 °C min^{-1}. Adsorption isotherms were determined using a Micromeritics ASAP 2020 gas adsorption analyzer at 77 K. X-ray photoelectron spectroscopy (XPS) was performed on a Thermo Fisher ES-CALAB 250Xi. Total organic carbon (TOC) was quantified using an Analytik Jena Multi N/C 3100 TOC analyzer. The chemical oxygen demand (COD) of flurbiprofen solutions before and after degradation was quantitatively determined using a UV-vis intelligent multi-parameter water quality tester, LH-3BA (Beijing Lianhua Science and Technology Development Co). Radical species were determined with a Bruker A300 EPR spectrometer. Electrochemical analysis was conducted on a CHI 660 E (CH Instruments, China) electrochemical workstation. The test conditions are detailed in Text S2.

For the mung bean germination experiment, 20 mung bean seeds were individually immersed in 50 mL of three distinct solutions: a blank control group (tap water), a flurbiprofen-contaminated group (20 mg L^{-1}), and an INC_{II} catalytic treatment group (flurbiprofen 20 mg L^{-1} + PMS 6 mM + catalyst 0.5 g L^{-1}, initial pH = 7.0, 298 K). After incubation under light-protected conditions for 12 h, all treatment groups were transferred to sterile Petri dishes lined with moistened gauze. During the experiment, the corresponding treatment solutions were replenished daily at pre-determined time intervals and in fixed quantities. The cultivation was performed at a constant temperature (25 ± 1 °C) and humidity (70 ± 5%) under complete darkness, with continuous observation for 5 days. The flurbiprofen removal efficiency was assessed by comparing germination rates and seedling growth parameters across the treatments.

Results and discussion

Catalyst characterizations

Fig. S1a and S1b are SEM images of cotton fibers with two crystalline structures at 2000 times magnification. Compared with C-I fibers, C-II fibers exhibit a slight degree of expansion, with a larger average diameter (18.33 μm *vs.* 17.61 μm). Thus, soaking in NaOH solution could lead to the expansion of cotton fibers. Fig. S1c is an SEM image of the dried mixture of carbonized C-II and NaCl. Compared with uncarbonized C-II in Fig. S1b, carbonized C-II fibers are broken into small fragments of 30 to 50 μm, surrounded by NaCl crystals. Meanwhile, NaCl crystals and carbonized C-II fragments are evenly mixed (Fig. S1c). The sizes of NaCl crystals range from 10 to 12 μm, which is significantly smaller than the typical size of 1 mm. The significantly reduced NaCl crystal size may be attributed to electrostatic interactions between the anions and cations in the IL with the NaCl crystal surface, which inhibited crystal growth among the carbonized cotton fibers. Fig. S1d displays the mixture of IL ([EMIm][$N(CN)_2$]), carbonized C-II, and NaCl. The obvious dark field is attributed to the IL, and small carbonized C-II fragments and NaCl crystals can be seen under the IL layer.

Fig. S2 displays the SEM image of the INC_{II} catalyst at a 40 μm scale. The fiber fragments in INC_{II} are further shortened to 20 to 35 μm compared with the mixture of carbonized C-II and NaCl in Fig. S1c. The shrunken cotton fibers can be attributed to pyrolysis and carbonization. As shown in Fig. 3c, the cavity within the cotton fiber remains intact even after calcination, without any signs of collapse. Fig. 3a–d present the detailed appearance of the INC_{II} catalyst, where the catalyst fibers are uniformly coated with graphene-like films. According to the XRD patterns of INC_{II} in Fig. 4, the films coated on the catalyst fibers are exactly graphene layers, which are at least 10 nm in thickness (Fig. 3b). Since monolayer graphene is 0.34 nm thick,[21] at least 30 graphene layers were coated on INC_{II} catalyst fibers. The catalyst fiber surface in Fig. 3a appears to be decorated with porous nanoparticles, potentially increasing its specific surface area. The multilayer graphene and nanoparticles adhered to the catalyst fibers can be ascribed to IL pyrolysis and the facilitating role of the NaCl template. The elemental mapping of the catalyst (Fig. 3e–g) reveals that the carbon matrix of the catalyst is uniformly doped with nitrogen. However, due to the limited amount or small size of multilayer graphene, pure graphene sheets were not detectable in the supernatant after the ultrasonic treatment of the INC_{II} catalyst. XPS testing quantified the nitrogen content as 16.37% (Table S3).

In addition, XRD was conducted to analyze the phase species of different INC_x catalysts. As shown in Fig. 4a, a series of peaks centered at 27.3°, 45.3°, 53.7°, and 56.3°, which are assigned to NaCl (JCPDS card No. 70-2509), are detected in the XRD patterns of INC_{II} and INC_{II}-UC catalysts, possibly resulting from the remaining NaCl template. According to the XRD patterns of various INC catalysts, NaCl was retained in the INC_{II}-UC catalyst, possibly due to the strong adsorption capacity of uncarbonized cotton fibers. Moreover, the broad and intense peaks centered at around 26.1° and 43.3° detected in all catalysts can be attributed to the (002) and (100) facets of hexagonal graphitic carbon in graphene.[22] The broad peak centered at 26.5° of pure graphene shows a leftward shift, which is typically ascribed to the "N defect" incorporated within the nitrogen-doped graphene. As nitrogen-doping increased interlayer spacing, the (002) diffraction peak showed a leftward shift.[21] The weaker (002) diffraction peak at 26.1° in the INC_{II} catalyst indicates that its graphene sheets are more disordered and less aggregated than those in other catalysts, increasing the surface area and active site exposure.[23] The elevated baseline in the XRD pattern of CC_{II} indicates the presence of amorphous material, along with the diffraction lines of graphite.[24] The peak of the (002) facet even shifts to near 23° in the XRD pattern of CC_{II}, indicating incomplete crystalline development and a larger *d*-spacing.[25] Meanwhile, the XRD patterns indicate that the NaCl template and carbonized cotton fibers can increase the amount and crystallinity of graphene sheets in INC_{II}. Fig. S3 displays the XRD patterns of INC_{II}-700 °C, INC_{II}, and INC_{II}-1100 °C. As the full width at half maximum of the peak represents the crystallization degree, the graphene sheets in INC_{II} exhibit the highest crystallization degree, which may facilitate electron transfer during PMS activation.

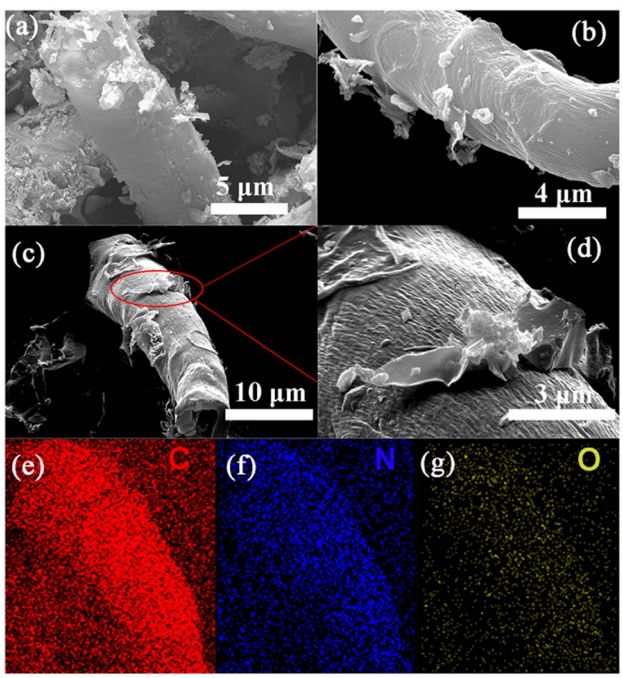

Fig. 3 SEM images of (a–d) INC_{II} catalyst; elemental mapping images of (e) C, (f) N, and (g) O in INC_{II}.

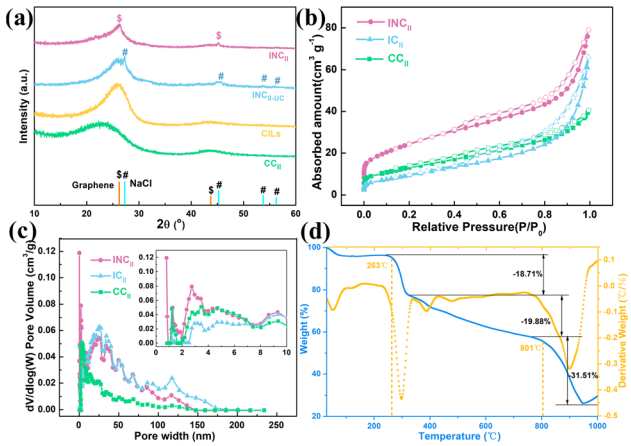

Fig. 4 (a) XRD patterns of CILs, CC_{II}, INC_{II-UC}, and INC_{II}; (b) N_2 sorption isotherms at 77 K (closed, adsorption; open, desorption) and (c) Barrett–Joyner–Halenda (BJH) pore size distributions of INC_{II}, IC_{II}, and CC_{II} catalysts; (d) TGA and DTG curves of INC_{II} precursor.

Fig. 4b and c display the N_2 sorption isotherms and pore size distribution of CC_{II}, IC_{II}, and INC_{II} catalysts to elucidate their detailed textural properties and inner structures. An obvious hysteresis loop and vertical tail of IC_{II} and INC_{II} catalysts revealed a typical Type H3 isotherm, demonstrating the presence of a certain portion of slit meso-and macro-pores (as proved in Fig. 3c). The BET surface areas of INC_{II}, IC_{II}, and CC_{II} catalysts (88.37, 36.04, and 47.30 $m^2\ g^{-1}$) indicated the pore-forming role of the NaCl hard template.[27] The inset in Fig. 4c shows that the pore sizes of the three catalysts range from 0 to 10 nm, and the INC_{II} catalyst has more micropores below

10 nm, contributing to a larger surface area. The TG-DTG curves indicate that the weight of the INC_{II} precursor decreases gradually with increasing temperature, exhibiting three stages from 30 °C to 1000 °C. The TGA curve in Fig. 4d first shows a slight weight loss below 100 °C, corresponding to the evaporation of guest-adsorbed water in the pores of the INC_{II} precursor. The pure IL [EMIm][$N(CN)_2$] decomposes at about 263 °C, and a maximum decomposition rate can be achieved at approximately 300 °C, resulting from the decomposition of imidazole cations.[28] Thus, the 18.71% weight loss at 260–300 °C (Fig. 4d) is ascribed to the decomposition of imidazole cations in the IL. Given that 801 °C is the melting temperature of the NaCl template, the final-stage weight loss at 760–950 °C is attributed to the decomposition of NaCl in the INC_{II} precursor.

Flurbiprofen degradation under nitrogen-doped multilayer graphene catalysts

Adsorption experiments were conducted on the three catalysts with various pyrolysis temperatures prior to flurbiprofen degradation (Fig. S4). The results indicate the low and negligible adsorption capacities of the three catalysts, with adsorption rates not exceeding 6%. To exclude the influence of adsorption, all catalysts were added to the flurbiprofen solution 0.5 h before PMS addition so that an adsorption equilibrium could be reached. The impact of catalyst quantity on flurbiprofen degradation efficiency was investigated. As depicted in Fig. S5, the flurbiprofen degradation efficiency at 90 min increases from 82.0% to 94.9% as the catalyst content increases from 0.4 g L^{-1} to 0.5 g L^{-1}. Thus, the flurbiprofen degradation efficiency increases progressively with increasing catalyst dosage. However, as the catalyst dosage increases further to 0.6 g L^{-1}, the degradation performance shows no improvement but rather a slight decline, possibly attributed to the mutual quenching of excess ROS within the system.[26] Consequently, 0.5 g L^{-1} INC_{II} was used for subsequent experiments. The influence of PMS concentration on flurbiprofen degradation efficiency was also evaluated. As illustrated in Fig. S6, the flurbiprofen degradation efficiency soars from 86.8% to 94.9% as the PMS concentration increases from 4 mM to 6 mM. Thus, the active sites of the INC_{II} catalyst were not fully saturated with PMS initially, and increasing PMS concentration accelerated flurbiprofen degradation. At a PMS concentration of 8 mM, a decrease in degradation efficiency was detected instead of further enhancement. Previous research indicated that excess PMS can result in the mutual quenching of ROS within the system, thereby diminishing the flurbiprofen degradation rate, as expressed in eqn (3)–(5).[26] Therefore, a PMS concentration of 6 mM was considered the most suitable for flurbiprofen degradation in this study and selected for subsequent experiments.

$$^{\cdot}SO_4^- + {}^{\cdot}SO_4^- \; 2SO_4^{2-} \quad (3)$$

$$HSO_5^- + {}^{\cdot}SO_4^- \; {}^{\cdot}SO_5^- + SO_4^{2-} + H^+ \quad (4)$$

$$HSO_5^- + {}^{\cdot}SO_4^- \; {}^{\cdot}SO_5^- + H_2O \quad (5)$$

Fig. 5a illustrates the flurbiprofen degradation performance of various catalysts. Evidently, the crucial raw materials significantly affect the PMS activation and flurbiprofen degradation capabilities. The absence of NaCl exerted the least influence on catalytic performance. In contrast, omitting the IL resulted in the most pronounced effect, which may be attributed to its high dosage and dual roles as a nitrogen and carbon source. Fig. 5b compares the degradation performance of the INC_{II} catalyst and two modified versions: one with carbonized C-I, and the other with uncarbonized C-II. Using uncarbonized C-II as the carbon source significantly reduced the catalytic performance. The fragmentation of C-II fibers caused by carbonization (Fig. S1c) resulted in small fragments that mixed more uniformly with NaCl. Thus, modifying C-I into C-II can slightly improve the PMS activation and flurbiprofen degradation performance. Fig. 5c presents the performance of different INC_{II} catalysts in activating PMS to degrade flurbiprofen. Evidently, 900 °C is the optimal carbonization temperature. The materials derived from the simple pyrolysis of the IL and C-II fibers demonstrated extremely poor efficacy. The flurbiprofen degradation performance surpasses all previously reported studies, as shown in Table S4. Fig. 5d depicts the influence of solution pH on the flurbiprofen degradation efficiency of the INC_{II} catalyst. Optimal flurbiprofen degradation was observed at neutral pH = 7. Approximately 90% of the flurbiprofen molecules are degraded within 90 min across a pH range of 3 to 7, signifying

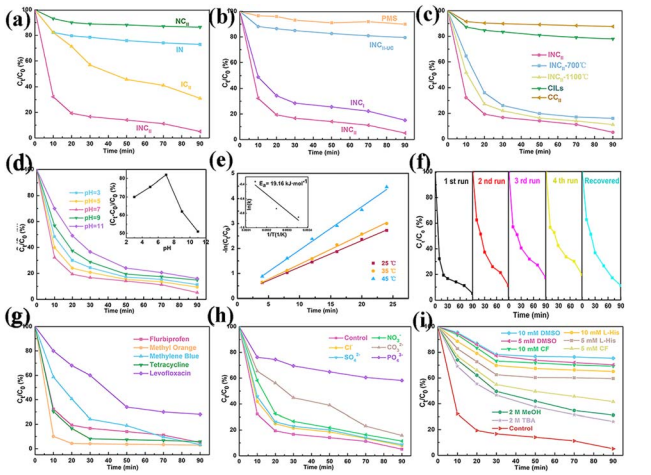

Fig. 5 (a) Comparison of catalytic performance of INC_{II}, IN, IC_{II}, NC_{II} in the presence of PMS; (b) comparison of flurbiprofen degradation with INC_{II}, INC_I, $INC_{II\text{-}UC}$, and PMS alone; (c) comparison of catalytic performance of diffrent INC_{II} catalysts, CILs, and CC_{II} in the presence of PMS; (d) effects of solution pH on flurbiprofen degradation by INC_{II} and the correlation between pH level and flurbiprofen conversion for 20 min (inset); (e) effects of reaction temperature on flurbiprofen degradation by INC_{II} and Arrhenius plot of ln(*k*) *versus* 1/*T* (inset); (f) cycles of catalytic flurbiprofen degradation by INC_{II} and regenerated catalyst; (g) flurbiprofen degradation at different contaminations of the INC_{II}/PMS system; (h) effects of high-concentration 0.01 M ions on INC_{II}/PMS system; (i) free radical quenching experiments (conditions: [flurbiprofen] = [tetracycline] = [levofloxacin] = 20 mg L^{-1}, [methylene blue] = [methyl orange] = 40 mg L^{-1}, [catalyst] = 0.5 g L^{-1}, [PMS] = 6 mM, pH = 7.0 unless otherwise noted).

the INC_{II} catalyst's robust catalytic performance in acidic environments. As the solution pH increased from 7 to 9, a significant decrease in flurbiprofen degradation efficiency was observed. Moreover, the degradation rate at an alkaline pH = 11 is substantially lower than at acidic conditions. The strongly alkaline solution could functionalize the surface of the nitrogen-doped carbon catalyst, possibly inducing electrostatic repulsion between the PMS anion and the catalyst. This repulsion impedes PMS adsorption and subsequent catalytic oxidative degradation, which is somewhat paradoxical since alkalinity is recognized to activate PMS.[27] In fact, the degradation rate was minimized at pH = 11. Solution pH significantly modulates the INC_{II} catalyst–flurbiprofen interaction and the degradation performance by regulating the surface charge properties of the catalyst, the structure of the electrical double layer (EDL), and the dissociation state of flurbiprofen functional groups. The protonation/deprotonation behavior of both sets of functional groups changed dynamically with pH variations. At low pH levels (<4), the carboxyl groups (–COOH) of flurbiprofen existed in a molecular form, leading to enhanced hydrophobicity. The nitrogen sites on the nitrogen-doped catalyst surface were protonated, carrying weak positive charges and resulting in a thinner EDL. Meanwhile, flurbiprofen and the catalyst predominantly exhibited hydrophobic interactions and π–π stacking, which facilitated flurbiprofen enrichment on the catalyst surface. At neutral pH levels (6 to 8), the –COOH groups of flurbiprofen were deprotonated to form $–COO^-$ (negatively charged), increasing the negative charge density on the catalyst surface and thickening the EDL. Electrostatic repulsion weakened flurbiprofen adsorption. However, PMS was readily activated by nitrogen sites to generate ROS, and coordination interactions partially compensated for the insufficient adsorption. At high pH levels (>10), flurbiprofen was fully dissociated into $–COO^-$, drastically increasing the surface negative charge density of the catalyst. The EDL thickened significantly, and strong electrostatic repulsion inhibited flurbiprofen adsorption, thereby shifting the reaction toward solution-phase radical oxidation.[28] In summary, pH determined the degradation efficiency by regulating interfacial interactions and activation pathways, and neutral pH levels were typically optimal.

Fig. 5e demonstrates the influence of reaction temperature on the flurbiprofen degradation by the INC_{II} catalyst, where increased temperatures promote flurbiprofen degradation. As the temperature rises from 25 °C to 45 °C, the flurbiprofen degradation rate constant (k) increases from 0.3644 min^{-1} to 0.8546 min^{-1}. The activation energy for flurbiprofen degradation by the INC_{II} catalyst (19.2 kJ mol^{-1}) was significantly lower than in most previous studies (30 kJ mol^{-1}) for catalyst/PMS/profen-drug systems.[29,30] The low activation energy indicates that the INC_{II} catalyst is favorable for catalytic degradation. The reusability test results in Fig. 5f confirm 90% flurbiprofen degradation within 60 min during the first run with INC_{II}. The catalytic activity remains largely unchanged throughout consecutive cycles. The fourth cycle still achieves nearly 80% flurbiprofen removal within 90 min, indicating the catalyst's stability and sustained activation. Following the fourth degradation cycle, the regenerated catalyst underwent heat treatment and recovered a portion of its activity. Its degradation efficiency reached 89.0% after 90 min, consistent with that of the second run. This activity recovery might be attributed to the evaporation of flurbiprofen and its intermediates, which were adsorbed onto the catalyst surface during degradation. The second pyrolysis removed such flurbiprofen and its intermediates from the catalyst surface, enabling catalytic activity recovery.[31,32] TOC and COD measurements were conducted on the flurbiprofen solution before and after degradation to assess the mineralization potential of the AOP based on $^{\bullet}SO_4^-$. The TOC and COD values and removal rates of INC_{II} catalyst/PMS systems after 90 min of degradation are presented in Table S2. The INC_{II}/PMS system achieved a TOC removal rate of 43.8% and a COD removal rate of 43.0% after 90 min of degradation, which were decent under equivalent concentrations of profen drugs and PMS.[33,34]

The degradation capabilities of the INC_{II}/PMS system for various dyes and antibiotics were investigated *via* degradation experiments using tetracycline, levofloxacin, methylene blue, and methyl orange as target substances. As shown in Fig. 5g, the degradation efficiencies of these dyes and antibiotics after 90 min of treatment are: 96.6% for methylene blue, 97.0% for methyl orange, 94.1% for tetracycline, and 72.0% for levofloxacin. The reduced levofloxacin degradation rate may be due to the limited ability of the catalytic system to break down the quinolone structure. Consequently, the INC_{II}/PMS system effectively degrades antibiotics (flurbiprofen and tetracycline) and cationic dyes (methyl orange and methylene blue). These results underscore the broad applicability of the INC_{II}/PMS system for wastewater treatment, including PPCP degradation. The practical applications of the INC_{II} catalysts were further evaluated by investigating the influence of various ions, such as Cl^-, SO_4^{2-}, PO_4^{3-}, CO_3^{2-}, and NO_3^-, on their performance.

Fig. 5h shows that all ions inhibit the degradation performance. Notably, CO_3^{2-} and PO_4^{3-} ions exert a more pronounced inhibitory effect on the catalytic process because CO_3^{2-} is a weak acid ion that readily forms HCO_3^- in water. Subsequently, HCO_3^- scavenges $^{\bullet}OH$ and $^{\bullet}SO_4^-$ radicals,[35] thereby impeding flurbiprofen degradation. CO_3^- also has a quenching effect on $O_2^{\bullet-}$.[36] Additionally, the hydrolysis of PO_4^{3-} in water tends to produce HPO_4^{2-} and OH^-, and the subsequent reaction of HPO_4^{2-} with $^{\bullet}OH$ and $^{\bullet}SO_4^-$ generates fewer reactive species ($^{\bullet}H_2PO_4$), declining the flurbiprofen removal rate.[37,38] In summary, although high concentrations of these ions did not significantly affect flurbiprofen degradation efficiency, individual ions exerted significant inhibitory effects. Overall, the nitrogen-doped carbon catalyst developed in this study offers significant benefits for environmental remediation in complex settings, which can withstand multiple cycles and address a diverse range of pollutants and ions.

The mechanisms of ROS generation from activated PMS to degrade flurbiprofen were systematically investigated through radical scavenging experiments with the flurbiprofen removal rate as an evaluation indicator. Methanol (MeOH), possessing α-H atoms, demonstrated efficacy in scavenging free sulfate radicals ($^{\bullet}SO_4^-$) and hydroxyl radicals ($^{\bullet}OH$) in the solution, with reaction rate constants of 3.2×10^6 M^{-1} s^{-1} and 9.7×10^8

M^{-1} s^{-1}, respectively. Additionally, TBA without any α-H atom exhibited a specific scavenging effect on free hydroxyl radicals, with a reaction rate constant of 7.6×10^8 M^{-1} s^{-1}.[39] As for $O_2^{\bullet-}$, scientists have exploited benzoquinone (BQ), CF, and CO_3^{-} as scavengers.[5,36,40] Numerous studies used BQ as an $O_2^{\bullet-}$ scavenger, while CO_3^{-} was least widely used, with a reaction rate constant below 9.0×10^8 M^{-1} s^{-1}.[36] The reaction rate constants of BQ for scavenging $O_2^{\bullet-}$ and $^{\bullet}OH$ are 1.1×10^9 M^{-1} s^{-1} and 1.2×10^9 M^{-1} s^{-1}, respectively, with no significant difference.[41] Therefore, CF was selected to scavenge $O_2^{\bullet-}$ in this work to avoid the interference of $^{\bullet}OH$. CF exhibits distinguishing reaction rate constants in scavenging $O_2^{\bullet-}$ and $^{\bullet}OH$ (2.3×10^8 M^{-1} s^{-1} and 5.4×10^7 M^{-1} s^{-1}, respectively). Additionally, CF rarely reacts with $^1O_2$, thereby avoiding disruptive scavenging of $^1O_2$. NaN_3, furfuryl alcohol (FFA), and L-histidine (L-His) were used to scavenge non-radical ROS $^1O_2$.[30,42,43] Similarly, the reaction rate constants of NaN_3 and FFA for $^{\bullet}OH/^{\bullet}SO_4^{-}$ are considerable or even higher than those for $^1O_2$.[44] Thus, L-His with a reaction rate constant of 2.3×10^7 M^{-1} s^{-1} for $^1O_2$ was selected to scavenge $^1O_2$ in this study. In addition to common ROS, DMSO was used (instead of methanol) to quench the surface-bound $^{\bullet}OH$ and $^{\bullet}SO_4^{-}$ species by reacting with them.[30,45] As shown in Fig. 5i, adding 2 M MeOH causes the flurbiprofen degradation efficiency to drop to 50.4% within 30 min. As 2 M TBA was added, the degradation efficiency decreased to 53.3% after 30 min. Thus, high concentrations of MeOH and TBA exhibit poor quenching effects on the degradation reaction, indicating that free $^{\bullet}SO_4^{-}$ and $^{\bullet}OH$ radicals in the solution play a relatively minor role during the reaction. Nevertheless, DMSO exhibits a strong quenching effect on the degradation reaction, demonstrating the importance of surface-bound $^{\bullet}OH$ and $^{\bullet}SO_4^{-}$ species during the degradation. In terms of $O_2^{\bullet-}$ and $^1O_2$ species, the quenching effects on the degradation reaction improved as the scavenger concentrations increased from 5 mM to 10 mM. However, Fig. 5i reveals that increasing the CF concentration results in a more pronounced quenching effect on the degradation reaction than that of L-His. Therefore, the system generates a greater amount of $O_2^{\bullet-}$ than $^1O_2$, indicating its more significant role in activating PMS to degrade flurbiprofen than $^1O_2$.

Identification of ROS in the INC_{II}/PMS system

The degradation mechanisms of the dye solution were further explored *via* EPR spectroscopy analysis using DMPO and TEMP as spin capture agents. Subsequently, the active substances in the INC_{II}/PMS system were investigated. As depicted in Fig. 6a, no signal is detected upon the addition of PMS at 0 min, suggesting the absence of active substances at the outset. As the reaction progressed, robust signals of DMPO-$^{\bullet}OH$ (1 : 2 : 2 : 1) and DMPO-$SO_4^{\bullet-}$ adducts appeared in the INC_{II}/PMS system, with escalating intensities over time. These results further confirmed that INC_{II} activated PMS to yield $^{\bullet}SO_4^{-}$ and $^{\bullet}OH$. The six-peak structure with intensities of 1 : 1 : 1 : 1 : 1 : 1 in Fig. 6b suggests the formation of $O_2^{\bullet-}$.[46] As shown in Fig. 6c, the TEMP capture agent also exhibits three characteristic peaks of $^1O_2$ at 1 : 1 : 1, implying $^1O_2$ generation during the reaction. A

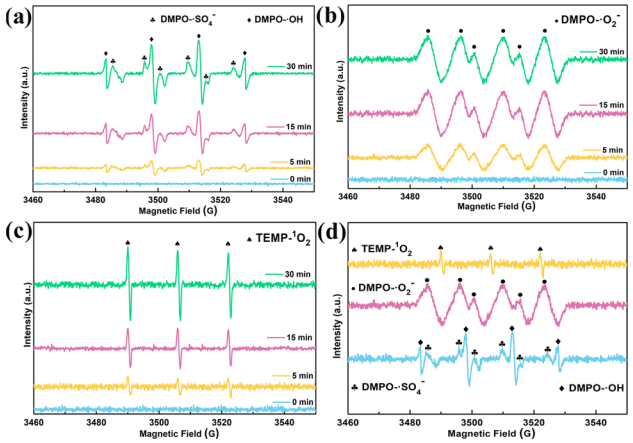

Fig. 6 EPR spectra of (a) DMPO-$^{\bullet}OH/^{\bullet}SO_4^{-}$, (b) DMPO-$^{\bullet}O_2^{-}$, (c) TEMP-$^1O_2$ adducts in the INC_{II}/PMS systems; (d) comparison of EPR spectra of different adducts after reaction for 30 min.

comparison of the reactive species intensities after 5 min of reaction (Fig. 6d) reveals that the DMPO-$O_2^{\bullet-}$ signal is the strongest, consistent with the radical quenching experiment results in Fig. 5i. Although the DMPO-$^{\bullet}OH$ (1 : 2 : 2 : 1) and DMPO-$SO_4^{\bullet-}$ adduct signals in Fig. 6d surpass those of TEMP-$^1O_2$, the radical quenching experiment suggests that free $^{\bullet}SO_4^{-}$ and $^{\bullet}OH$ radicals play relatively minor roles in the degradation process. This may be attributed to the brief half-life of $^1O_2$ (merely 10^{-11} s), leading to its rapid depletion in EPR tests. Moreover, this does not contradict the inferred vital role of catalyst-surface-bound $^{\bullet}OH$ and $^{\bullet}SO_4^{-}$ species from the radical quenching experiment.

The presence of electron-transfer mechanisms within the system was validated *via* a series of electrochemical assays. The response of the electrical circuit during the reaction of the INC_{II}/PMS system was examined by analyzing open-circuit potential (OCP) data, time–current curves (*i*–*t* curves), and linear sweep voltammetry (LSV) profiles. Insights into electron-transfer pathways were derived from the OCP test results. As depicted in Fig. 7a, the steady potential of INC_{II} in an aqueous environment is 0.55 V. Following PMS introduction, the stable-state potential gradually increased to 0.96 V over 1000 s due to the activation effect of PMS. Electron adsorption from INC_{II} to PMS facilitates a swift transfer, forming a metastable intermediate complex (INC_{II}/PMS*), which, in turn, boosts the potential at the catalyst surface. Subsequently, the added flurbiprofen served as an electron donor and induced a potential decline to 0.87 V, indicating that the INC_{II}/PMS* complex extracted electrons from flurbiprofen, resulting in a potential reduction.[47] Using the INC_{II} catalyst as the working electrode, the sequential addition of PMS and flurbiprofen yields distinct negative and positive current spikes, respectively (Fig. 7b). The steady-state current of INC_{II} in an aqueous environment was approximately 0 A. Following PMS introduction, the steady current rose almost instantly to 6 μA due to the activation effect of PMS. The electron adsorption of INC_{II} onto PMS facilitated rapid electron transfer, thereby enhancing the current on the catalyst surface.

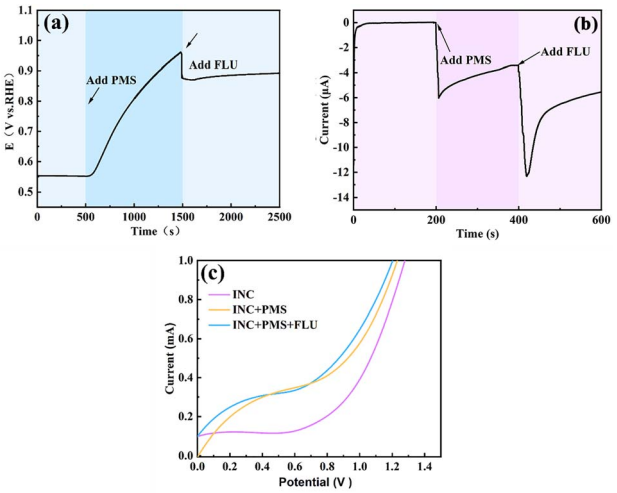

Fig. 7 OCP curve (a), *i*–*t* curve (b), and LSV curve (c) measured with INC_{II} catalyst-modified glassy carbon electrode under the set conditions. Reaction conditions: $[K_2SO_4]$ = 0.1 M, [PMS] = 6 mM, [flurbiprofen] = 20 mg L^{-1}.

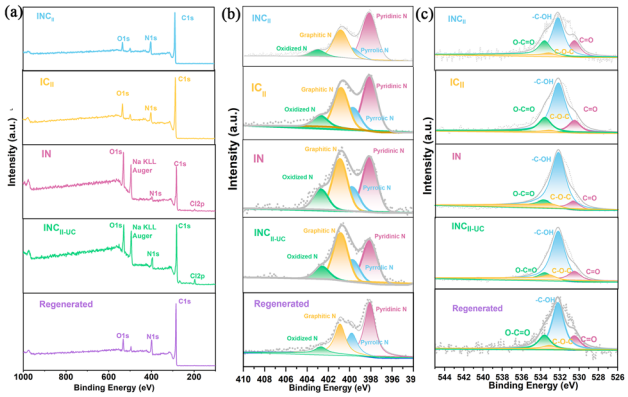

Fig. 8 XPS spectra of INC_{II}, IC_{II}, IN, $INC_{II\text{-}UC}$, and regenerated INC_{II} catalysts: survey spectra (a), N 1s (b), and O 1s (c).

Over time, the catalyst on the electrode surface was gradually reacted, causing a slight current loss in 200 s. Subsequently, introducing flurbiprofen (an electron donor) caused the current to surge again. Therefore, the INC_{II}/PMS* complex extracted electrons from flurbiprofen, intensifying the current. These findings corroborate that INC_{II} can activate PMS directly, consistent with experimental evidence, and verify the occurrence of electron-transfer processes within the INC_{II}/PMS/flurbiprofen system. The LSV test results are presented in Fig. 7c. Using an INC_{II} electrode, a significant current response was observed in the pure electrolyte, confirming its favorable conductivity. Adding PMS to the electrolyte induced a negligible intensity fluctuation in the current signal. However, the subsequent flurbiprofen introduction leads to a sharp increase in current intensity, indicating an enhanced reaction between the INC_{II} catalyst and PMS, ultimately inducing electron transfer. The pronounced current intensity escalation post-flurbiprofen addition can be ascribed to the consumption of reactive radicals by flurbiprofen and its potentially direct electron transfer with the catalyst surface.[48] The chronoamperometric, LSV, and OCP test results collectively indicate an electron transfer pathway intrinsic to the INC_{II}/PMS/flurbiprofen system.

The elemental composition and chemical states of five catalysts derived from modified cotton fibers and metal-free IL were characterized by XPS. Fig. 8a–c show the survey XPS spectra, N 1s, and O 1s XPS spectra of the five catalysts, respectively. Fig. 8a reveals the presence of C, N, and O in all five catalysts. The Auger peaks of Na KLL in the IN and INC_{II}-UC catalysts may result from residual NaCl template during synthesis. The elemental composition of different catalysts is displayed in Table S3. The INC_{II} catalyst has a high nitrogen doping level of 16.37%. A previous study demonstrated that pyridinic, pyrrolic, and graphitic nitrogen can serve as active sites for PMS activation in nitrogen-doped carbon catalysts.[49] However, no definitive nitrogen species has been demonstrated as more favorable for the radical or non-radical pathway. Pyridinic nitrogen could conjugate with the freely mobile π electrons in nitrogen-doped carbon catalysts, thereby altering charge distribution and facilitating the decomposition of adsorbed PMS into $^1O_2$.[50] In addition, Lewis bases with lone-pair electrons (*e.g.*, pyridinic nitrogen, pyrrolic nitrogen, and C=O groups) are more conducive to the radical pathway. More scholars considered pyrrolic nitrogen as conducive to free radical generation (*e.g.*, $^{\bullet}OH$ and $^{\bullet}SO_4^-$) by absorbing the O–O sites of PMS.[51] Many scientists believe that the excellent electrical conductivity of graphitic nitrogen is favorable for non-radical electron transfer pathways.[52] This study identified pyridinic nitrogen as the most active site, based on the relative abundance of different nitrogen species and their corresponding degradation performance. For further clarification, the optimal INC_{II} catalyst was regenerated *via* secondary pyrolysis at 900 °C after four reaction cycles. Table S5 shows decreased content of both pyridinic and graphitic nitrogen. The slightly declined performance of the regenerated INC_{II} catalyst compared to the first run (Fig. 5f) may be attributed to the minor reduction in pyridinic nitrogen content. Considering the radical-scavenging experiment results (Fig. 5i), pyridinic nitrogen is more advantageous for the radical pathway, promoting the generation of $O_2^{\bullet-}$ and catalyst-surface-bound $^{\bullet}OH$ and $^{\bullet}SO_4^-$.[50] The relatively low levels of $^1O_2$ and electron transfer, as indicated by the results of radical scavenging, electrochemical, and EPR experiments (Fig. 5i, 6d, and 7), may be ascribed to the limited contribution of the non-radical pathway, presumably due to the low graphitic nitrogen content in INC_{II}. Furthermore, C=O groups can also serve as active sites for PMS activation in non-metallic nitrogen-doped carbon catalysts.[53] The C=O groups can be oxidized during degradation, and the electron-transfer intermediates or lone pairs generated on Lewis basic sites can, in turn, increase the electron density of adjacent carbon rings and enhance pollutant degradation. This study identified C=O groups as the most active sites among other oxygen-containing groups, based on the relative content of different oxygen-containing species and their corresponding degradation performance (Table S6 and

Fig. 5a and b). Analysis of the O 1s spectra of unused and regenerated INC_{II} catalysts (Fig. 8c and Table S6) reveals a C=O content decrease in the regenerated catalyst. Thus, the C=O groups functioning as active sites are oxidized by ROS during degradation and depleted.[54] The increase in C–O groups and decrease in O–C=O groups in the O 1s spectrum of the regenerated catalyst may be attributed to their transformation during secondary pyrolysis.

Proposed degradation pathway and toxicity evaluation

Currently, few have studied the flurbiprofen degradation pathway. Thus, the degradation intermediates involving the INC_{II} catalyst/PMS system were analyzed by LC-MS. Based on the *m*/*z* values, 10 compounds were identified using positive ion mode ESI, and the mass spectra of the intermediates are displayed in Fig. S7. This study proposed six probable flurbiprofen degradation pathways according to the products (Fig. 9). In pathway I, ROS preferentially attacked the electron-rich carboxyl carbon, releasing a methanol molecule to form product P1. In pathway II, ˙OH attacked the ortho and para positions of the F benzene ring. In pathway III, the electron-rich F group on the benzene ring was oxidized to a –OH group. Subsequently, the substituent at the *meta*-position of the hydroxyl group was oxidized to form products P6 to P9. Alternatively, the para position of the –OH group on the benzene ring was attacked by ˙OH, adding a new –OH group to form products P11 and P12. In pathway IV, the para position of the F benzene ring was attacked by ˙OH, adding a new –OH group. Then the –F group and the branch on the benzene ring were oxidized to form products P11 and P12, which normally require higher energy to overcome steric and polarity effects than *via* pathway III.[55] In pathway V, the methylene of the branch on the benzene ring was lost owing to C–C bond cleavage, thereby forming product P13. In pathway VI, the branch on the benzene ring was directly oxidized to a –OH group, forming product P16, also with high energy requirements.[55] In conclusion, the main reactions involved in flurbiprofen transformation across all pathways were hydroxylation, oxygenation, substitution, cleavage, and other eliminations, without rearrangements or additions. Unfortunately, none of the pathways showed cleavage of biphenyls in flurbiprofen, which affected the degree of mineralization and the toxicity of the degradation intermediates. Notably, Fig. S7 shows that 6 out of the 10 identified compounds have incorporated –SO_3 ionic fragments during mass spectrometry, which are likely derived from the PMS molecule. This finding clearly confirms the vital role of catalyst-surface-bound ˙SO_4^- related species in degradation, as demonstrated by the radical scavenging experiments (Fig. 5i).

The toxicity of flurbiprofen and its degradation intermediates was predicted using TEST. As shown in Fig. 10a, although a small number of intermediates (*e.g.*, P2, P5, P6, P10, P11, and P13) in the INC_{II} catalyst/PMS system increase the oral median lethal dose (LD_{50}) index in rats, most significantly decrease it. As shown in Fig. 10b, all degradation pathways result in lower developmental toxicity in the final products (P1 to P17) compared to the parent compound (flurbiprofen). Fig. 10c and d indicate that flurbiprofen degradation is accompanied by a reduction in bioaccumulation and mutagenic toxicity, and its intermediates show a distinct downward trend in mutagenic toxicity. The LD_{50} and bioconcentration toxicity of P11, P16, and P17 are higher than that of flurbiprofen. However, the concentration of these intermediates may not be significant according to the intensity of the product fragment peaks in Fig. S7. Furthermore, degradation pathway VI involves the direct oxidation of the branch of the benzene ring to a –OH group, which demands greater chemical energy and is, therefore, less

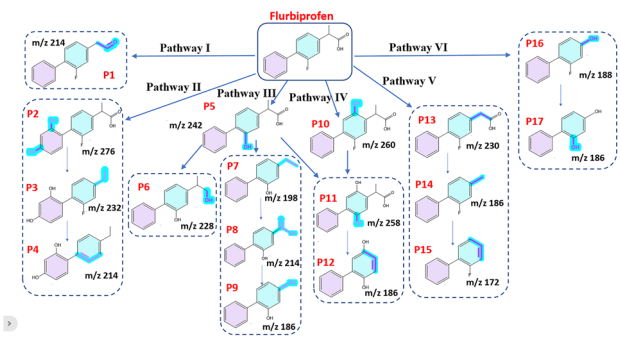

Fig. 9 Proposed flurbiprofen degradation pathways in the INC_{II} catalyst/PMS solution.

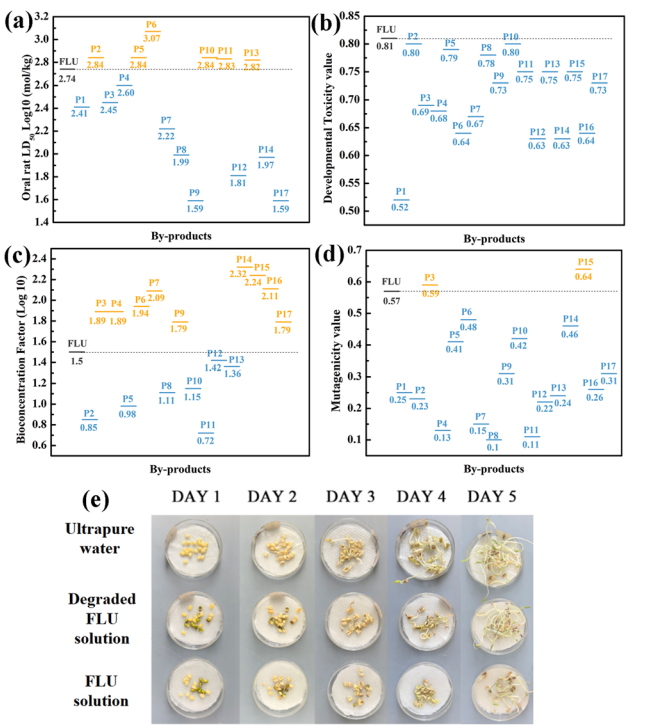

Fig. 10 Toxicity evaluation of flurbiprofen and its intermediates after degradation for 30 min. (a) Oral rat LD_{50}, (b) developmental toxicity, (c) bioaccumulation factor, (d) mutagenicity of flurbiprofen and its degradation intermediates in the INC_{II} catalyst/PMS system, and (e) (g) mung bean growth under tap water, degraded flurbiprofen solution, and untreated flurbiprofen (5 days). Conditions: [flurbiprofen] = 20 mg L^{-1}, [PMS] = 6 mM, [catalyst] = 0.5 g L^{-1}, [pH] = 7, [T] = 25 °C.

likely to occur. Thus, the formation of the more toxic intermediates P16 and P17 was prevented. Consequently, the environmental pollution risks may be further reduced. The comprehensive assessment shows decreasing toxicity in most flurbiprofen intermediates over time. The mung bean cultivation experiment showed that all beans germinated and grew successfully in the flurbiprofen solution following PMS activation. Thus, the reaction system is green and efficient, and its potential for practical applications in wastewater treatment is validated.

Conclusions

This study developed a nitrogen-doped multilayer graphene catalyst derived from modified cotton fibers, with sodium chloride as the template and the nitrogen-containing IL [EMIm][$N(CN)_2$] as the nitrogen source. The optimal nitrogen-doped graphene catalyst, INC_{II}, demonstrated superior activity for PMS activation to degrade flurbiprofen, achieving a removal rate of approximately 94.9% at an initial concentration of 20 mg L^{-1}, surpassing all previous works. This INC_{II} catalyst has also exhibited excellent adaptability, stability, and versatility under various conditions. The flurbiprofen degradation pathway was elucidated, and the catalyst/PMS system exhibited low toxicity and good environmental compatibility. The intermediates showed the unprecedented adsorption of active $^{\cdot}SO_4^-$ related species on the catalyst surface. EPR and radical quenching experiments revealed surface-bound $^{\cdot}SO_4^-$ related active species and $O_2^{\cdot-}$ as the primary reactive species. Effective electron transfer was found among INC_{II}, PMS, and flurbiprofen surfaces. Pyridinic nitrogen was identified as the most potent active site for PMS activation. By applying waste cotton fibers, this study presents a practical pathway for biomass recycling.

Author contributions

Sun Rui: writing – original draft, visualization, resources, conceptualization. Chen Yanfei: resources, conceptualization. Limeng Yang: writing – review & editing, visualization, conceptualization. Zhu Zhi: writing – review & editing, conceptualization. Zheng Zhaohua: visualization, writing – review & editing. Sun Li: resources, methodology, conceptualization, funding acquisition.

Conflicts of interest

There are no conflicts to declare.

Data availability

The data that support the findings of this study are available from the corresponding author.

Supplementary information (SI): texts concluding the analytical methods of HPLC-MS, the electrochemical analysis tests, and some figures and tables. See DOI: https://doi.org/10.1039/d5ra09729k.

Acknowledgements

We appreciate the financial support from the Natural Science Basic Research Program of China (No. 81672742).

Notes and references

1 C. Yi, Q. Liao, W. Deng, Y. Huang, J. Mao, B. Zhang and G. Wu, *Sci. Total Environ.*, 2019, **684**, 527–536.
2 L. Yang, T. Wang, Y. Zhou, B. Shi, R. Bi and J. Meng, *Sci. Total Environ.*, 2021, **760**, 144080.
3 S. Kar, T. Mandal and G. Halder, *Process Saf. Environ. Prot.*, 2024, **188**, 877–904.
4 G. R. Peyton, *Mar. Chem.*, 1993, **41**, 91–103.
5 S. Wang, J. Kang, P. Yan, J. Shen, J. Zuo, Y. Cheng, L. Shen, B. Wang, S. Zhao and Z. Chen, *Appl. Catal., B*, 2024, **342**, 123419.
6 A. Ali, D. J. Jasim, N. Rakhimov, M. J. Mohammed, M. M. Karim, A. H. Athab, A. Kumar, N. Ahmad and L. Guo, *J. Mol. Struct.*, 2025, **1319**, 139373.
7 M. A. Younis, S. Manzoor, A. Ali, L. Guo, M. I. Yousaf, S. Nosheen, A. Naveed and N. Ahmad, *Dalton Trans.*, 2024, **53**, 1809–1816.
8 T. Rasheed, M. T. Anwar, D. B. Ferry, A. Ali and M. Imran, *Environ. Sci.: Water Res. Technol.*, 2023, **10**, 12–28.
9 T. Rasheed, T. Ahmad, S. Khan, D. B. Ferry, F. Sher, A. Ali and S. Majeed, *Environ. Monit. Assess.*, 2023, **195**, 1142.
10 T. Aziz, A. Farid, F. Haq, M. Kiran, N. Ullah, S. Faisal, A. Ali, F. U. Khan, S. M. You, A. Bokhari, M. Mubashir, L. F. Chuah and P. L. Show, *Environ. Res.*, 2023, **222**, 115253.
11 Z. Wang, B. Liu, C. Ji, L. Tang, B. Huang, L. Feng and Y. Feng, *J. Hazard. Mater.*, 2023, **448**, 130905.
12 B. Qiu, C. Pan, W. Qian, Y. Peng, L. Qiu and F. Yan, *J. Mater. Chem. A*, 2013, **1**, 6373–6378.
13 H. Zhang, Y. Ling, Y. Peng, J. Zhang and S. Guan, *Inorg. Chem. Commun.*, 2020, **115**, 107856.
14 S. Ghosh, N. A. Kouame, L. Ramos, S. Remita, A. Dazzi, A. Deniset-Besseau, P. Beaunier, F. Goubard, P.-H. Aubert and H. Remita, *Nat. Mater.*, 2015, **14**, 505–511.
15 Y. Yuan, L. Yang, B. He, E. Pervaiz, Z. Shao and M. Yang, *Nanoscale*, 2017, **9**, 6259–6263.
16 L. Xiao, Y. Huang, Y. Luo, B. Yang, Y. Liu, X. Zhou and J. Zhang, *ACS Sustain. Chem. Eng.*, 2018, **6**, 14759–14766.
17 W. Yang, L. Yang, Y. Yang, C. Fu, C. Sheng and P. Zhang, *Cellulose*, 2024, **31**, 3221–3242.
18 Y. Zhang, H. Zhang, J. Yao, Y. Song, W. Li and X. Xuan, *Chem. Eng. J.*, 2024, **483**, 149326.
19 L. Miao, H. Duan, Z. W. Wang, Y. K. Lv, W. Xiong, D. Z. Zhu, L. H. Gan, L. C. Li and M. X. Liu, *Chem. Eng. J.*, 2020, **382**, 122945.
20 Z. L. Zhu, X. B. Yang, X. Ye, Q. L. Li, J. Q. Wang, L. Wu, Z. H. Huang and M. X. Wang, *Sep. Purif. Technol.*, 2024, **346**, 127456.
21 L. Qu, Y. Liu, J.-B. Baek and L. Dai, *ACS Nano*, 2010, **4**, 1321–1326.

22 X. Wang, H. Zhang, H. Lin, S. Gupta, C. Wang, Z. Tao, H. Fu, T. Wang, J. Zheng, G. Wu and X. Li, *Nano Energy*, 2016, **25**, 110–119.
23 W. R. Zhong-Shuai Wu, L. Wen, L. Gao, Z. C. Jinping Zhao, G. Zhou, F. Li and H.-M. Cheng, *ACS Nano*, 2010, **4**, 3187–3194.
24 K. Strickland, M. W. Elise, Q. Y. Jia, U. Tylus, N. Ramaswamy, W. T. Liang, M. T. Sougrati, F. Jaouen and S. Mukerjee, *Nat. Commun.*, 2015, **6**, 7343.
25 M. Q. Zhong, S. Chen, T. Wang, J. X. Liu, M. Mei and J. P. Li, *J. Mol. Liq.*, 2022, **354**, 118902.
26 D. Zheng, J. Zou, H. Xu, M. Wu, Y. Wang, C. Feng, E. Zheng, T. Wang, Y. Shi, Y. Chen and B. Li, *Chemosphere*, 2023, **325**, 138387.
27 C. D. Qi, X. T. Liu, J. Ma, C. Y. Lin, X. W. Li and H. J. Zhang, *Chemosphere*, 2016, **151**, 280–288.
28 Y. Yang, L. Yang, Q. Zhang, Y. Li, L. Cao, Q. Li, C. Fu, C. Sheng, S. Zhang, H. Xie and P. Zhang, *Chem. Eng. J.*, 2026, **527**, 171819.
29 B. E. Channab, M. El Ouardi, S. E. Marrane, O. A. Layachi, A. El Idrissi, S. Farsad, D. Mazkad, A. BaQais, M. Lasri and H. A. Ahsaine, *RSC Adv.*, 2023, **13**, 20150–20163.
30 V. Thai, T. B. Nguyen, C. W. Chen, C. Huang, R. A. Doong, L. J. Chen and C. D. Dong, *Sep. Purif. Technol.*, 2024, **334**, 126033.
31 J. L. Xie, L. R. Zhang, X. Luo, L. Huang, X. B. Gong and J. Tian, *Chem. Eng. J.*, 2023, **457**, 141149.
32 J. L. Xie, X. F. Pan, C. M. Jiang, L. Zhao, X. B. Gong and Y. Liu, *Environ. Res.*, 2023, **236**, 116745.
33 M. Zhang, H. Tao, C. Zhai, J. Yang, Y. Zhou, D. Xia, G. Comodi and M. Zhu, *Appl. Catal. B Environ. Energy*, 2023, **326**, 122399.
34 S. H. Lee, S. Annamalai and W. S. Shin, *Environ. Pollut.*, 2023, **322**, 121023.
35 B. Byambaa, E.-J. Kim, M. G. Seid, B.-M. An, J. Cho, S. L. Aung and K. G. Song, *Chem. Eng. J.*, 2023, **456**, 141037.
36 X. Cheng, H. Guo, Y. Zhang, X. Wu and Y. Liu, *Water Res.*, 2017, **113**, 80–88.
37 K. Wang, P. Xiang, R. S. Zhou, M. T. Huang and P. S. Lin, *J. Water Proc. Eng.*, 2023, **54**, 104043.
38 Z. F. Meng, R. X. Mo, Q. Wang, K. W. Zheng, W. Li and C. Q. Qin, *Colloids Surf., A*, 2023, **662**, 130984.
39 G. Wang, Y. Liu, X. Dong and X. Zhang, *J. Hazard. Mater.*, 2022, **437**, 129357.
40 L. Yang, W. Chen, C. Sheng, H. Wu, N. Mao and H. Zhang, *Appl. Surf. Sci.*, 2021, **549**, 149300.
41 X. Y. Zhao and Z. H. Zhang, *Environ. Sci. Technol.*, 2025, **59**, 5913–5924.
42 X. Hu, H. Hu, X. Yan, R. Feng, T. Li, W. Zhou, F. Wei and Y. Bai, *Chem. Eng. Sci.*, 2025, **302**, 120791.
43 Y. Luo, C. Liu, S. Kang, C. Ji, B. Lai, W. Zhang, J. Li and Y. Ren, *J. Hazard. Mater.*, 2025, **489**, 137606.
44 Y. H. Luo, C. Liu, S. R. Kang, C. H. Ji, B. Lai, W. M. Zhang, J. Li and Y. Ren, *J. Hazard. Mater.*, 2025, **489**, 137606.
45 Y. Yao, C. Lian, G. Wu, Y. Hu, F. Wei, M. Yu and S. Wang, *Appl. Catal., B*, 2017, **219**, 563–571.
46 J. Yan, C. Chen, H. Sun, X. Su and S. Zhang, *Environ. Sci. Pollut. Res.*, 2023, **30**, 37475–37486.
47 X. Zheng, X. Niu, D. Zhang, M. Lv, X. Ye, J. Ma, Z. Lin and M. Fu, *Chem. Eng. J.*, 2022, **429**, 132323.
48 X. Zhang, B. Xu, S. Wang, X. Li, C. Wang, B. Liu, F. Han, Y. Xu, P. Yu and Y. Sun, *Chem. Eng. J.*, 2022, **431**, 133477.
49 X. Zhao and Z. Zhang, *Environ. Sci. Technol.*, 2025, **59**, 5913–5924.
50 X. Chen, W.-D. Oh, Z.-T. Hu, Y.-M. Sun, R. D. Webster, S.-Z. Li and T.-T. Lim, *Appl. Catal., B*, 2018, **225**, 243–257.
51 S. Liu, S. Yin, Z. Zhang, L. Feng, Y. Liu and L. Zhang, *J. Hazard. Mater.*, 2023, **441**, 129905.
52 Z. Luo, Y. Xu, D. Tang, L. Lu, Y. Li, M. Zhang and J. Sun, *Sep. Purif. Technol.*, 2023, **326**, 124769.
53 Z. Meng, R. Mo, Q. Wang, K. Zheng, W. Li and C. Qin, *Colloids Surf., A*, 2023, **662**, 130984.
54 B. Lu, F. Wu, Z. Yin, C. He, J. Qian, Y. Mao, X. You, G. Lin, X. Yang and B. Huang, *Appl. Surf. Sci.*, 2023, **640**, 158308.
55 K. Bonnot, P. Benoit, L. Mamy and D. Patureau, *Crit. Rev. Environ. Sci. Technol.*, 2022, **53**, 47–69.